Scanning Microscopy

Volume 1993
Number 7 *Physics of Generation and Detection of Signals Used for Microcharacterization*

Article 13

1993

Synchrotron Radiation Induced X-Ray Microanalysis: A Realistic Alternative for Electron- and Ion-Beam Microscopy?

K. Janssens
University of Antwerp, Belgium

F. C. Adams
University of Antwerp, Belgium

M. L. Rivers
Brookhaven National Laboratory, New York

K. W. Jones
Brookhaven National Laboratory, New York

Follow this and additional works at: https://digitalcommons.usu.edu/microscopy

Part of the Biology Commons

Recommended Citation

Janssens, K.; Adams, F. C.; Rivers, M. L.; and Jones, K. W. (1993) "Synchrotron Radiation Induced X-Ray Microanalysis: A Realistic Alternative for Electron- and Ion-Beam Microscopy?," *Scanning Microscopy*: Vol. 1993 : No. 7 , Article 13.
Available at: https://digitalcommons.usu.edu/microscopy/vol1993/iss7/13

This Article is brought to you for free and open access by the Western Dairy Center at DigitalCommons@USU. It has been accepted for inclusion in Scanning Microscopy by an authorized administrator of DigitalCommons@USU. For more information, please contact digitalcommons@usu.edu.

Scanning Microscopy Supplement 7, 1993 (Pages 191-208) 0892-953X/93$5.00+.25
Scanning Microscopy International, Chicago (AMF O'Hare), IL 60666 USA

SYNCHROTRON RADIATION INDUCED X-RAY MICROANALYSIS: A REALISTIC ALTERNATIVE FOR ELECTRON- AND ION-BEAM MICROSCOPY?

K. Janssens*, F.C. Adams, M.L. Rivers[1], K.W. Jones[1]

Department of Chemistry, University of Antwerp (U.I.A.)
Universiteitsplein 1, B-2610 Wilrijk/Antwerp, Belgium
[1]Department of Applied Science, Brookhaven National Laboratory,
Upton, Long Island, New York 11973, USA

Abstract

Synchrotron radiation induced X-ray micro fluorescence analysis (μ-SRXRF) is compared with more conventional microanalytical techniques such as secondary ion microscopy (SIMS) and electron probe X-ray microanalysis (EPXMA) for two typical microanalytical applications. μ-SRXRF and EPXMA are employed for the analysis of individual particles, showing the complementary character of both techniques. By means of element mapping of trace constituents in a heterogeneous feldspar material, the strong and weak points of μ-SRXRF in comparison to EPXMA and SIMS are illustrated. The most striking difference between μ-SRXRF and the other two microanalytical methods is the ability of SRXRF to probe deep into the investigated material, whereas SIMS and EPXMA only investigate the upper surface of the material. The possibilities of μ-SRXRF using radiation from bending magnets of third generation synchrotron rings are briefly discussed. μ-SRXRF is considered to be a valuable method for the analysis of major, minor and trace elements which can be used profitably in parallel with electron- and ion-beam methods.

Key Words: Synchrotron radiation, trace elemental mapping, individual particle analysis, micro X-ray fluorescence, environmental analysis, geological analysis, lateral resolution, trace element analysis, secondary ion mass spectrometry, electron probe X-ray microanalysis.

*Address for correspondence:
Koen Janssens
Dept. of Chemistry, Univ. of Antwerp (U.I.A.),
Universiteitsplein 1,
B-2610 Antwerp/Wilrijk, Belgium
Phone No.: +32 3 828.23.73
Fax No.: +32 3 828.23.76

Introduction

During the last decade, a number of microanalytical methods have come into existence which are capable of yielding information on the lateral distribution of elemental species in solid materials. A number of these methods and some of their properties are listed in Table 1. A few of these techniques are the microscopic analogues of bulk analytical methods which have been in use for a much longer time and have opened new horizons in an already established field. Such is the case for synchrotron radiation induced X-ray fluorescence (SRXRF). Conventional (tube-excited) XRF analysis, either in its energy-dispersive (ED) or wavelength dispersive (WD) form, is a widespread analytical method which allows for reliable multielement analysis of bulk specimen at the ppm level.

The use of synchrotron radiation for XRF work was initiated by Sparks (Sparks *et al.*, 1980). In the last 5 years, as a result of the increasing availability of electron storage rings as sources of highly intense, collimated and polarized X-rays in the energy range between 1 and 30-40 keV, around the world, a number of X-ray fluorescence microprobes have been constructed. At Hasylab (Hamburg, FRG) and at the NSLS (National Synchrotron Light Source; Brookhaven National Laboratories, Upton, NY, USA), white light microprobes are in operation (Bavdas *et al.*, 1988; Jones and Gordon, 1989). Using collimated pencil beams, sensitive trace element mapping with minimum detection limits in the 1-10 ppm range can be performed with a lateral resolution of the order of 10 μm. At SRS (Daresbury, UK), at SSRL (Stanford, CA, USA) and at the Photon Factory (Tsukuba, Japan), focussed monochromatic microbeams are employed (Van Langevelde *et al.*, 1990; Thompson *et al.*, 1988; Goshi *et al.*, 1987).

As can be seen from Table 1, μ-SRXRF represents a unique combination of qualities which cannot be found in any of the other microanalytical methods listed, the most important one being its potential for yielding reliable quantitative information. As with secondary ion microscopy (SIMS), μ-SRXRF is capable of trace level microanalysis but does not have any of the disadvantages

Table 1. Characteristics of various microanalytical techniques (adapted from Traxel, 1988).

	Projectile	Quantum Energy (keV)	Destructive?	Spot Size (μm)	Penetration Depth (μm)	MDL (ppm)	Accuracy
SIMS	M^+, N^-	10-30	yes	< 1	0.010	< 1	w.t. 10%
LAMMA	hν		yes	~ 1	1	~ 1	w.t. 50%
μ-PIXE	p^+, α	2-3 x 10^3	y/n	0.3	5-100	5-10	b.t. 10%
EPXMA	e^-	5-100	no	< 0.1	1-5	> 100	b.t. 20%
μ-SRXRF	X	10-50	no	3-15	10-1000	1-100	b.t. 5%

SIMS = secondary ion microscopy; LAMMA = laser microprobe mass analysis; PIXE = particle induced X-ray emission; EPXMA = electron probe microanalysis; μ-SRXRF = synchrotron radiation induced X-ray micro flourescence analysis; b.t. = better than; w.t. = worse than.

associated with a destructive mass spectrometric technique such as SIMS or LAMMA (laser microprobe mass analysis). Combining sensitive elemental mapping with the proven accuracy and reliability of quantitative XRF makes μ-SRXRF a very interesting analytical technique. Since SIMS and μ-SRXRF are based on very different microbeam-matter interactions, making an objective comparison on other than the overall performance of the methods is difficult.

A more detailed comparison can be made when μ-SRXRF is considered next to its closest analogues: μ-PIXE (particle induced X-ray emission) and EPXMA (electron probe X-ray microanalysis). Essentially, these three methods only differ in the type of energy carriers that are being used in the microbeam; all are based on the creation of inner shell vacancies in target atoms and rely on the detection of the resulting element specific radiation using energy-dispersive Si(Li) detectors (many cases in EPXMA also use wavelength-dispersive detectors). The strong and weak points of μ-SRXRF can be seen from a consideration of the production efficiencies of photon-, electron- and proton-induced X-radiation emission as a function of atomic number and particle energy. Figure 1 shows that for infinitely thick targets, at excitation energies below 20 keV, the photon induced X-ray emission yield is about a factor of 10 to 100 higher than that corresponding to electron- or proton-based excitation. This means that per characteristic X-ray produced, the energy deposition in the sample using μ-SRXRF is at least a factor of 10-100 lower than in the case of EPXMA; this difference is even larger in the case of μ-PIXE since virtually all energy of the MeV ions is deposited into the sample without creating an inner-shell vacancy (Mazzolini *et al.*, 1981; Vis, 1988). A second important difference between photon- versus electron- or proton-induced X-ray production is the dependence of the production cross sections on the target atomic number Z. As can be seen in Figure 1, in the case of charged particles, the production efficiencies decrease with rising Z whereas they increase in the case of photon excitation. As a result, EPXMA and μ-PIXE are very suitable for the determination of low-Z elements whereas μ-SRXRF is more appropriate for visualising distributions of species of higher atomic number. In a comparison between μ-PIXE and μ-SRXRF, for the analysis of biological specimen, van Langevelde *et al.* (1990) concluded that for Z > 20 (Ca), the monoenergetic (15 keV) X-ray microprobe at SRS provides better MDL (minimum detection limit) values than a proton microprobe. A clear advantage of μ-PIXE is that it can readily be combined with other ion-beam analytical techniques such as, e.g., RBS (Rutherford backscattering) and STIM (scanning transmission ion microscopy) which provide information on

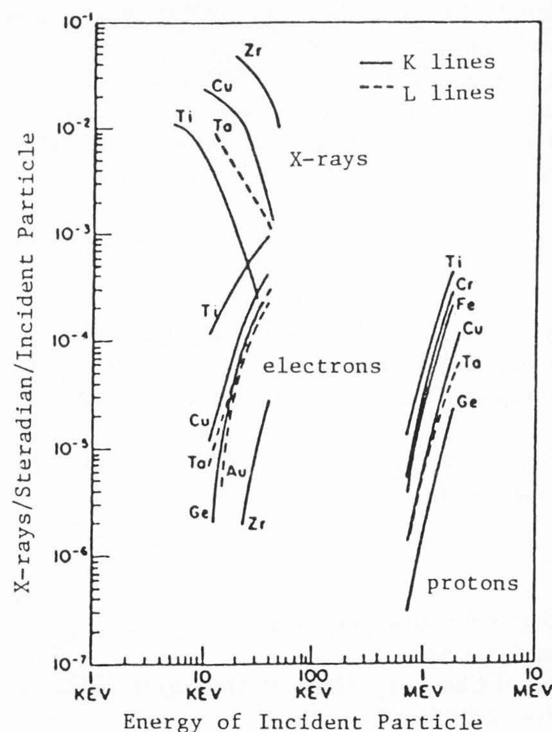

Figure 1. Quantum efficiency of photon, electron and proton induced X-ray emission (adapted from Birks *et al.*, 1964)

the low-Z matrix and the internal structure of the material under study, respectively. Another possibility is to combine PIXE with PIGE (proton induced gamma emission), with which low-Z elements (such as Li, Be, B, F) can also be determined. Similarly, μ-SRXRF can be combined with XANES (X-ray absorption near-edge structure) and CMT (computer-aided microtomography) measurements yielding information on the oxidation state of chemical species (Janssens *et al.*, 1993a) and on the three-dimensional distribution of specific elements or of the density within a sample (Spanne and Rivers, 1987), respectively. Another similarity between μ-SRXRF and μ-PIXE is that both techniques involve fairly large, expensive and technically complicated installations for generating the beams of primary exciting particles. In contrast, LAMMA, EPXMA and SIMS experiments can be performed in laboratory scale instruments and are accessible to many well-equipped analytical laboratories.

Another important difference between the interaction of photons and charged particles (such as protons and electrons) with matter is the probability for scatter interactions. As a result of many (in)elastic encounters, the retardation of energetic charged particles into solids gives rise to the presence of a bremsstrahlung continuum in the detected X-ray spectra. In the case of X-ray fluorescence, each primary photon only undergoes one or two scattering interactions with the sample atoms before it is either absorbed (photo-ionisation) or escapes from the solid. This results in nearly background-free XRF spectra in case monochromatic photon excitation is employed and yields (sub)ppm level detection limits for selected elements (van Langevelde *et al.*, 1990). Only in the region at and just below the primary energy, (in)coherent scatter peaks significantly contribute to the background. In the case of white light excitation, a continuous scatter background can be observed in SRXRF spectra. The linear polarisation of synchrotron radiation in the plane of the storage ring can be employed advantageously to decrease the background level when the Si(Li) detector is positioned in this plane at 90° to the incident beam. This effect makes it possible to achieve ppm level MDL values with μ-SRXRF employing polychromatic excitation (Jones and Gordon, 1989). μ-SRXRF has an additional major benefit in that, in contrast to charged particle techniques, sample materials need not be placed in vacuum and need not be conducting; the penetrating nature of the X-rays facilitates the use of wet cells and similar devices for *in vivo* type of measurements.

In the past, a number of papers have been published in which the qualities of SRXRF are compared for bulk analysis with PIXE (Bos *et al.*, 1984; van Langevelde *et al.*, 1990), with tube-excited XRF (Jones *et al.*, 1984; Bos *et al.*, 1984) and with radio-isotope excited EDXRF (Baryshev *et al.*, 1987; Török *et al.*, 1989). In a previous paper (Janssens *et al.*, 1992a), we have compared the use of a monochromatic and a polychromatic X-ray microprobe to that of an electron- and proton microprobe for individual particle analysis. This study, which involved the analysis of standard NIST (National Institute for Science and Technology) glass microspheres, revealed large differences in the analytical qualities of the two X-ray microprobes. In terms of speed of analysis and achievable detection limits, the white light X-ray microprobe at NSLS and the electron microprobe proved to be the most appropriate for characterisation of large numbers of individual particles. Using the white light X-ray microprobe, MDL values for, e.g., Ca and Fe were found to be 10 and 2 ppm, respectively, in 20 μm particles for a 100 sec counting interval. This study also revealed that the NSLS X-ray microprobe is limited to analysing particles with diameters larger than ~5 μm.

As a continuation of these investigations, the first part of the present work discusses the analysis of a "real" particle set using EPXMA and white beam μ-SRXRF. Individual aerosol particles collected on the Antarctic during the summer and winter of 1988 were analysed in order to assess the composition and relative importance of the various aerosol sources in this remote area. Antarctica is supposed to suffer minimally from anthropogenic pollution, although the concentrations of several trace gases are known to be increasing over this continent. The recent interest in the Antarctic atmosphere has resulted in a recognition of the need for detailed aerosol characterisation studies (Bodhaine *et al.*, 1987). The (dis)advantages of the two analytical methods in terms of speed of analysis, sensitivity and their ability to classify particles into various classes are discussed.

Next to the analysis of minute samples such as micrometeorites, aerosols and water-suspended particulate matter, μ-SRXRF can also be employed for visualising the distribution of elemental species in larger samples. This type of measurement involves the scanning of the microbeam over a selected area of the sample surface while signals originating from each location are collected and sorted accordingly. Published reports mainly deal with investigations in the biological and geological field (see, e.g., Frantz *et al.*, 1988; Kwiatek *et al.*, 1987; Jones *et al.*, 1992). Usually, thin sections of minerals, or tissues are studied, and lateral resolutions approximately equal to the dimensions of the photon beam are achieved. From a general analytical point of view, however, it is also of interest to compare the performance of μ-SRXRF when non-thin samples are studied; a large number of industrially interesting materials such as ceramics are either too brittle or too sensitive to allow elaborate sample preparation procedures to

be used; the latter can also be a source of contamination (see below).

In the second part of this work, μ-SRXRF is compared with SIMS and EPXMA for elemental mapping of major and trace constituents in a thick sample of a feldspar mineral. This material was studied because of its microheterogeneity both at the major and at trace levels. Attention is devoted to the lateral resolution attainable in the elemental maps and the factors that influence it and to the sensitivity of the various techniques.

Finally, the predicted analytical qualities of an μ-SRXRF station which may be installed in the next few years at a beam line of a third generation X-ray source such as the European Synchrotron Radiation Facility (ESRF), now under construction in Grenoble, France, will be briefly discussed.

Materials and Methods

The Antarctic aerosols were first collected during the summer and winter of 1988 at the Brazilian Antarctic station "Commandante Ferraz", on the Admiral Bay, Antarctic Peninsula. The sampling site is located 1 km from the main station and is 300 m from the sea. Details of the sampling procedure can be found in Artaxo *et al.* (1990). Coarse particles (with diameter > 2 μm) were collected on Nuclepore 8.0 μm pore size filters. An electron micrograph of a few NaCl microcrystals found on these filters is shown in Figure 2.

The particles were sized and analysed using a Jeol JXA-733 Electron Prube X-ray Microanalyser (Jeol Ltd., Tokyo, Japan) equipped with a Tracor Northern TN2000 computer and energy-dispersive detection system. All samples were excited with an electron beam current and voltage of 1 nA and 25 kV, respectively. An automated particle sizing and analysis program was used to locate and collect X-ray data from about 500 particles per sample (Raeymaekers *et al.*, 1986). In this routine, the electron beam is scanned over a selected area of the filter. A particle is detected when the back-scattered electron signal exceeds a chosen threshold. For each particle, the coordinates of the particle's perimeter are determined, yielding its mean diameter. Then, the electron beam is positioned at the geometric center of the particle, and an energy-dispersive X-ray spectrum is collected for each particle. In view of the large amounts of raw data which may be collected in this way, the spectra are evaluated on-line in a semi-quantitative way; relative abundances of the elements present in the particles can be calculated from the peak areas. Per particle, the program takes about 40 sec to perform all the above mentioned manipulations; usually analyses of this type are run overnight. Within the 500 analysed aerosol particles, approximately 100 were found to have a diameter > 5 μm. Only the latter data were used in this work. In order to reveal the various classes the particles fall into, the resulting data matrix (particle number versus X-ray intensities of all elements found in each particle) are subjected to hierarchical cluster analysis using Ward's error sum strategy (Van Espen, 1984); in view of the limited accuracy of the on-line spectrum evaluation step, the clustering is executed in normalised X-ray intensity space rather than in concentration space (Bernard *et al.*, 1986; Janssens *et al.*, 1988).

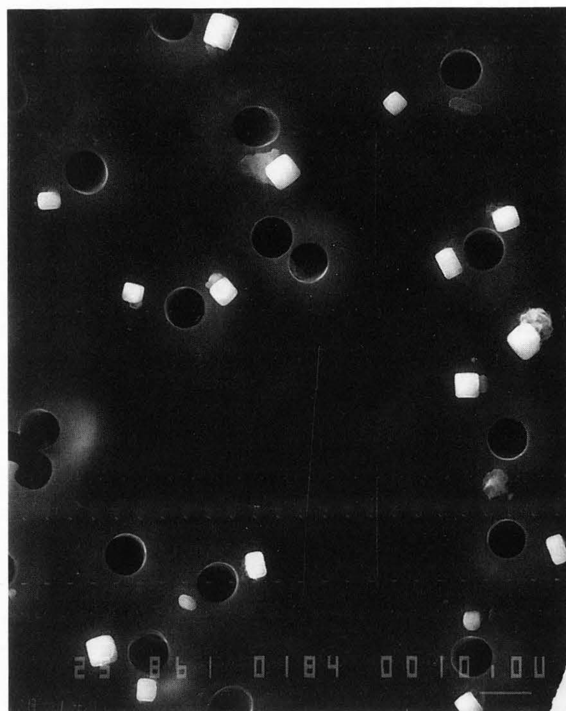

Figure 2. NaCl microcrystals on a Nuclepore filter sampled in the Antarctic. Pore diameter is 8 μm.

For the X-ray microprobe experiments, the instrument at the X26A beamline of the NSLS was employed. After emerging from the storage ring UHV (ultra high vacuum), the beam is defined by four Ta slits and further collimated by a 5 x 5 or an 8 x 8 μm^2 crossed slit system. The sample is positioned at 45° to the incoming beam. The polychromatic energy spectrum impinging on the sample has a maximum of about 10^4 photons/sec/eV/mA/μm^2 near 8 keV. Soft X-rays (E < 4 keV) are heavily absorbed by the Be-end windows of the beam pipe and the air path between the collimator slits and the sample. The specimen is viewed by a horizontally mounted stereozoom binocular microscope, equipped with a TV camera. For the analysis of individual particles, an 8 x 8 μm^2 collimator was employed to define the beam size. X-ray spectra were collected by

locating a particle on the filter using the microscope, moving it into the beam and maximizing the detectable count rate. This process takes about 1 to 2 min/particle. Per particle, spectrum collection times between 100 and 900 sec were employed. In contrast to the EPXMA instrument, all above mentioned manipulations were executed manually, making the measurements a very time-intensive undertaking. About 3 h of instrument time were devoted to each filter; in this period, ~30 particles could be analysed on each sample. The X-ray data obtained from each particle were processed in the same way as was done for the EPXMA data. Clustering of the particles in normalised X-ray intensity space also proved to yield a better group separation than in concentration space. Correlations between the trace-element constituents within the various groups is studied by means of principal component analysis.

For the elemental mapping experiments, a specific 100 x 100 μm^2 area of a grain of Carnmenellis Granite was studied. The perthitic matrix of this material consists of Na (albite) and K rich feldspar phases. The overall major and trace composition of the two minerals (Goossens *et al.*, 1989) is listed in Table 2. Details on the origin of the material can also be found in this reference.

The grain was imbedded in orthodontic resin, cut, and the resulting surface polished to 1 μm using diamond paste. The surface was then gold-coated for SIMS analysis. By rastering the 30 kV O^- beam over a 250 x 250 μm^2 area and locally removing the gold coating by ion sputtering, a rectangular area of the underlying mineral was exposed, showing a large (30 x 100 μm^2) albite exsolution lamella in a ground mass of K-feldspar, as shown in Figure 3.

In this area, elemental maps were collected, first by EPXMA, then by μ-SRXRF and finally by SIMS. During the μ-SRXRF experiment, a collimator yielding a 5 x 5 μm^2 photon beam was employed. The collection of the 512 x 512 SIMS maps took about 2 h of instrument time, including the alignment of the ion-optical system. The collection of the K and Na X-ray maps (140 x 200 pixels) using EPXMA took about 1 h. The synchrotron radiation induced X-ray images were collected using a dwell time of 50 sec per pixel; X-ray images of 25 x 35 pixels in size were collected taking a total instrument time of about 12 h to acquire.

For the evaluation of the electron- and photon-induced X-ray spectra, the AXIL (analysis of X-ray spectra by iterative least squares) code was employed (Van Espen *et al.*, 1986). For the purpose of quantifying the trace element contents of the Antarctic aerosol samples, thin target sensitivity values were experimentally determined for a number of elements by means of NIST SRM's (standard reference materials) 1832 and

Table 2. Average bulk composition of albite and K-feldspar phase in microcline perthite (adapted from Goosens *et al.*, 1989).

	K-feldspar matrix	exsolution lamellae
	Matrix (EPMA) (%)	
Na_2O	0.6 %	11
Al_2O_3	18.9 %	20.1
SiO_2	64.7 %	68
K_2O	16.6 %	0.22
CaO		0.17
	Traces (SIMS) (ppm)	
Li_2O	13	0.9
Rb_2O	840	3.0
SrO	480	9.5
Cs_2O	7.9	0.14
BaO	48	3.2

Figure 3. Backscattered electron image of microcline perthite. Horizontal field width is 300 μm. Albite exsolution (dark) lamellae in a K-feldspar matrix (light) are visible. Dimensions of large lamella parallel and perpendicular to black line are approximately 30 x 140 μm.

1833. On the basis of the polychromatic excitation spectrum emerging from the NSLS storage ring, a theoretical sensitivity curve was calculated and scaled to the experimental values, providing interpolated sensitivity values

Table 3. Characteristics of the various particle classes found by heirarchical clustering of elemental electron and photon induced X-ray intensities of the Antractic Aerosol particles.

	EPXMA		μ-SRXRF	
	group abundance (%)	group composition (% X-ray intensity)	group abundance (%)	group composition (% X-ray intensity)
	41	Cl (95), Na (5)	51	Cl (70), S (1), Br (1)
S	28	Cl (34), S (29), Mg (28), K (23)	14	Cl (28), Ca (20), S (2)
U	14	Cl (71), S (15), Mg (11)		
M	10	Ca (46), S (47)	10	Ca (54), S (2), Sr (1)
M	4	Si (37), Cl (23), Fe (11),		
E		Al (8), Mg (7), S (5), K (4)	7	Fe (70)
R	3	Si (56), Al (22), K (12), Cl (6)		
	55	Cl (92), Na (6), S (1), Ca (1)	45	Cl (80), K (3), Ca (3), Br (2)
W	25	Cl (87), Na (5), K (1), Ca (1)		
I	7	Cl (76), S (10), K (5), Na (4), Ca (3)		
N	5	Cl (57), S (17), Mg (9)		
T	5	S (36), Cl (25), K (20), Mg (8), Ca (8)	37	Cl (54), K (4), Ca (20), S (3),
E				Br (3), Sr (1), Cu (0.5), Zn (0.5)
R	3	Cl (75), Mg (22), S (2)	18	Br (25), Cl (13), K (12),
				Ca (11), Zn (10), S (1), Ni (1)

for the elements not present or certified in SRM's 1832 and 1833. The concentration of the trace elements in the Antarctic aerosol particles was determined by assuming an NaCl matrix and by correcting for attenuation of the incoming and emerging X-rays.

Individual Particle Analysis

The results of the cluster analysis of the electron- and photon-induced X-ray data derived from the Antarctic aerosol samples are summarized in Table 3. The discrepancy between the abundance of the various classes can be attributed to the fact that only a limited number of particles could be analysed with μ-SRXRF (60 particles in total) within the available beamtime. The most important fraction of the particles consists of sea-salt aerosol (see Figure 2), showing the characteristic cubical morphology of halite microcrystals. This is similar to the results obtained by Artaxo *et al.* (1990) for samples collected in the same location during 1985-1987. Other classes found are soil dust and sulphate particles. In both the EPXMA and the μ-SRXRF data, the seasonal differences between summer and winter aerosols are evident. The summer data show unreacted NaCl microcrystals, freshly formed as the result of bubble

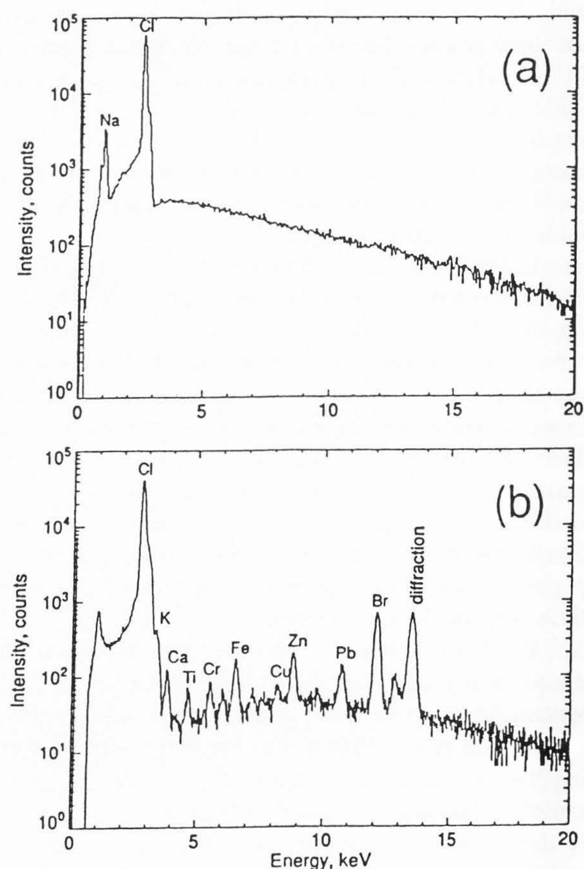

Figure 4. Energy dispersive X-ray spectra of the NaCl microcrystals shown in Figure 2. (**a**) Electron induced X-ray spectrum, showing characteristic peaks of matrix elements; (**b**) synchrotron radiation induced XRF spectrum, showing trace element lines.

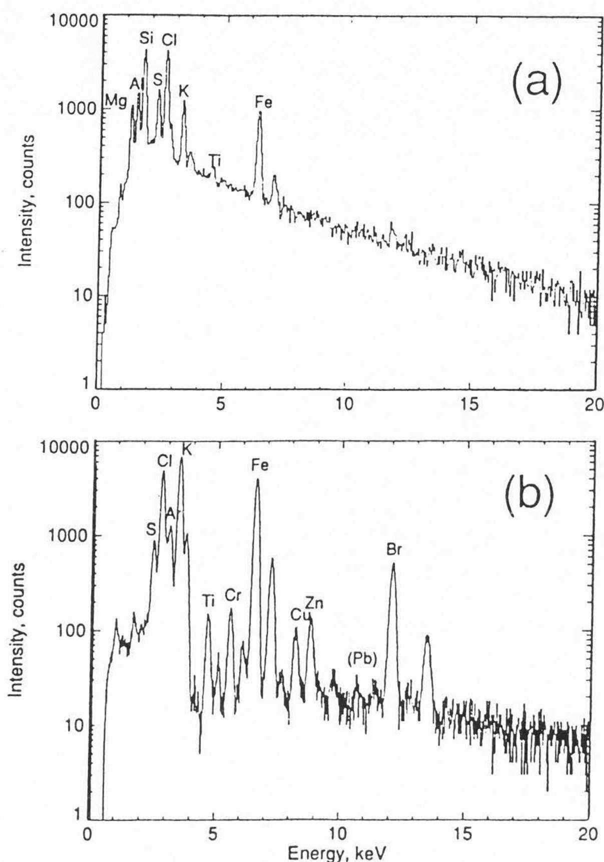

Figure 5. X-ray spectra of soil dust particles obtained by means of (**a**) EPXMA, (**b**) μ-SRXRF.

bursting. In the winter sample, the Cl-rich particles also contain appreciable amounts of S and Ca and are the result of secondary reactions between marine aerosols and trace gases. EPXMA and μ-SRXRF spectra of a particle belonging to the NaCl class (summer sample) are shown in Figure 4 and clearly illustrate the complementarity of the two methods. Whereas in the electron-induced spectrum (Figure 4a), only the major elements (Na and Cl) are visible in the μ-SRXRF spectrum; also, information on minor and trace constituents such as Ca, Ti, Cr, Fe, Cu, Zn, Br, Rb and Pb is available. For example, the Pb signal in Figure 4b corresponds to a concentration of about 25 ppm. The MDL value for Pb is approximately 5 ppm in this case. On the other hand, the sensitivity of the μ-SRXRF instrument for low-Z elements (e.g., Na, Mg, Al, Si) is very low compared to that of EPXMA, making it hard even to identify the major elements of the soil dust class of aerosols, as shown in Figure 5. This low sensitivity is the result of both the small production cross section for and the considerable absorption of soft fluorescent X-rays such as Na-K_α and Mg-K_α in the μ-SRXRF

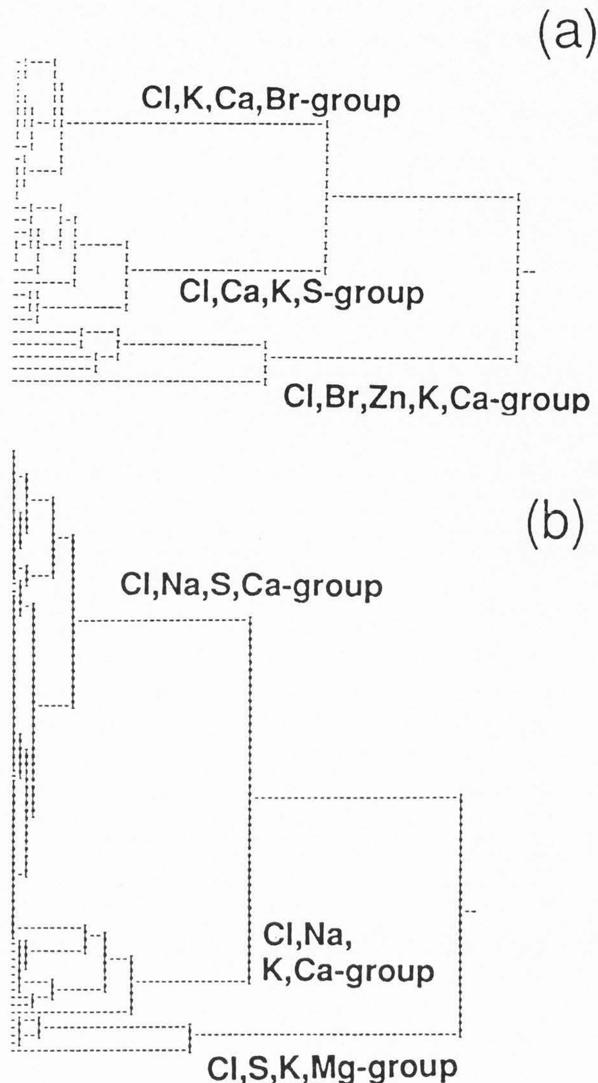

Figure 6. Cluster of diagrams of X-ray data derived from the Antarctic winter aerosols using (a) μ-SRXRF, (b) EPXMA.

spectrometer. Despite the fact that EPXMA and μ-SRXRF feature almost complementary sensitivity versus atomic number characteristics, it is remarkable that very similar cluster diagrams are obtained. As an example, in Figure 6, the dendrograms derived from the EPXMA and μ-SRXRF data for the winter sample are shown. In both cases, three major groups of particles are readily discernable; in the EPXMA case, however, the Na and Mg signals serve to split up the Cl-rich group into subclasses. A detailed examination of the μ-SRXRF data on the Cl-rich group in the summer data show two subgroups featuring an average S content of 0.43 $\pm$ 0.02 and 0.53 $\pm$ 0.05 %w, respectively. As also reported by Artaxo *et al.* (1990), a large variability is

Table 4. Concentrations of selected minor and trace constituents of NaCl microcrystals (see text for details). Values are expressed in ppm unless otherwise indicated.

	S (%)	K	Ca	Fe	Zn	Br	Sr	Pb
1	0.43	65	300	14	5	41	8	9
2	0.39	112	54	17	2	87	39	26
3	0.41	-	14	7	2	21	2	24
4	0.45	54	10	19	2	109	7	15
5	0.40	32	14	87	1	50	-	6
6	0.42	-	71	19	2	34	13	11
7	0.46	55	280	32	5	114	5	65
8	0.44	-	67	17	1	45	3	27
9	0.46	-	125	5	6	32	5	150
10	0.42	96	38	14	4	54	-	26
Average	0.43	41	97	23	3	59	8	36
Standard deviation	0.02	41	106	24	2	33	11	43

found in the concentration of the trace elements within each particle group. As an illustration, Table 4 lists the concentrations of a few trace elements in a number of the particles belonging to one of the above mentioned Cl-rich subgroups; the particles, having diameters in the 12-15 μm range, all showed the same cubical morphology and had a nearly identical major and minor composition (see sulphur data in Table 4). The concentrations in Table 4 were calculated assuming a NaCl matrix; the thicknesses of the NaCl microcrystals were estimated from the dimensions of the top face of the particles. Figure 7 shows the result of performing principle component analysis on the complete NaCl group of particles in the summer sample. The loadings of the major and trace constituents are plotted in the space of the first two principal components. A strong correlation between K, Ca and Sr is found; this correlation is also found in the winter samples. The K, Ca correlation is normally found in Antarctic bulk aerosol samples but does not always occur in the analysis of individual particles. Using factor analysis, other workers (Artaxo *et al.*, 1993) have also noted the Ca, Sr correlation (both elements belong to group IIa of the periodic system) but have found that K and Ca were associated with different sea-derived factors. They also attribute part of the potassium abundance to a soil-derived component. Other correlated elements in the μ-SRXRF data are Cr, Ni, Cu, Zn and Pb. This correlation may be indicative of the presence of an anthropogenic aerosol source.

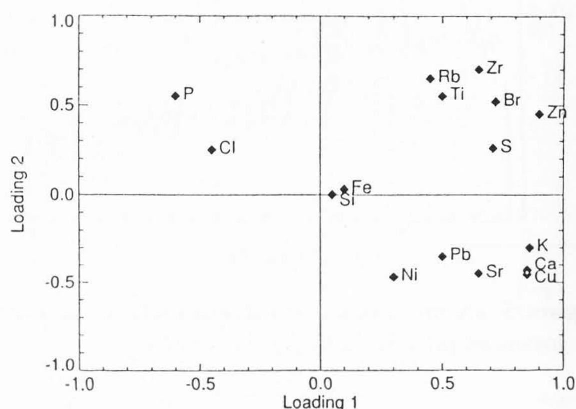

Figure 7. Loading plot of trace elements on the first two principal components derived from X-ray data on the Cl-rich aerosols found in the summer sample.

Trace Element Imaging

In Figures 8, 9 and 10, elemental maps are shown of various elements in the perthite material collected using electron, ion and X-ray microscopy, respectively. Figure 9 illustrates the applicability of SIMS for mapping the distribution of most elements in the periodic table; the Na and K distribution are found to be complementary, while most of the minor and trace constituents (except Ca) are concentrated in the K-rich phase. In the Al and Si maps none of the structure obtained in the other images is found.

A similar pattern is found in the EPXMA images (Figure 8), although only maps of the major elements could be collected. Using μ-SRXRF, again a wide range of trace constituents can be mapped; however, no data on low-Z elements below K could be obtained under the experimental conditions employed. Similar to the electron and photon induced X-ray spectra of the aerosol particles discussed above (see Figures 4 and 5), large difference can be observed between the X-ray spectra derived from the Na and K rich phases using EPXMA and μ-SRXRF. As can be seen in Figures 11a

Figure 8. Electron induced X-ray maps of the large exsolution lamella shown in Figure 3. (**a**) Na-K_{α}, (**b**) K-K_{α}.

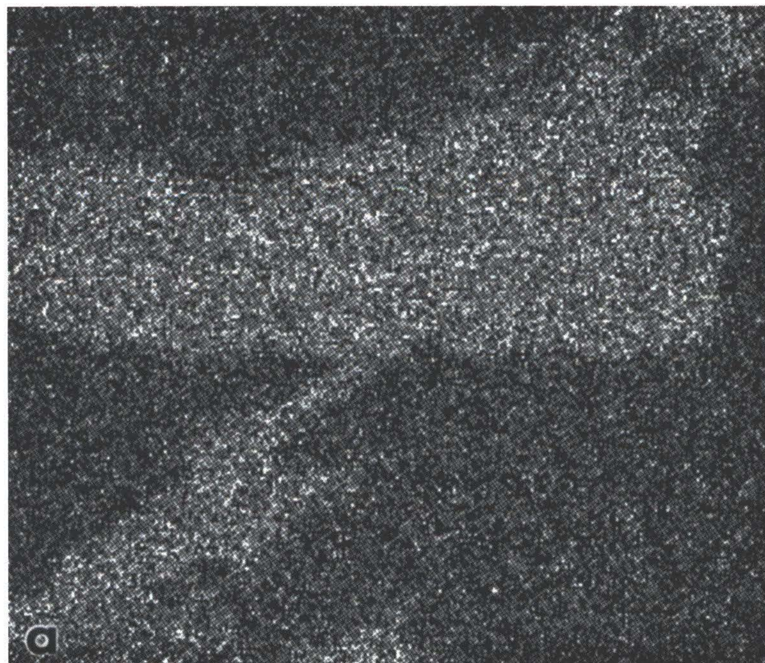

and 11c, only the major constituents of the minerals (Al, Si, K, Na) are visible in the electron induced spectra. In contrast, the μ-SRXRF spectra (Figures 11b and 11d) collected at approximately the same locations on the sample show an abundance of characteristic peaks. A number of these originate from the gold coating used during the sample preparation (Au, Pt). Others (e.g., Mn, Fe, Pb, Sr, Rb), however, correspond to the trace and minor constituents of the perthite mineral. However, the relative abundance of, e.g., Rb among the two phases is clearly not in agreement with the concentration data for this element listed in Table 2. The reason for this discrepancy becomes clear when the elemental maps of K and Rb are considered as collected with SIMS and μ-SRXRF (Figures 9 and 10, respectively). Whereas in the SIMS images, irrespective of the element/mass being considered, all images show the same two-phase distribution, in the μ-SRXRF images, this

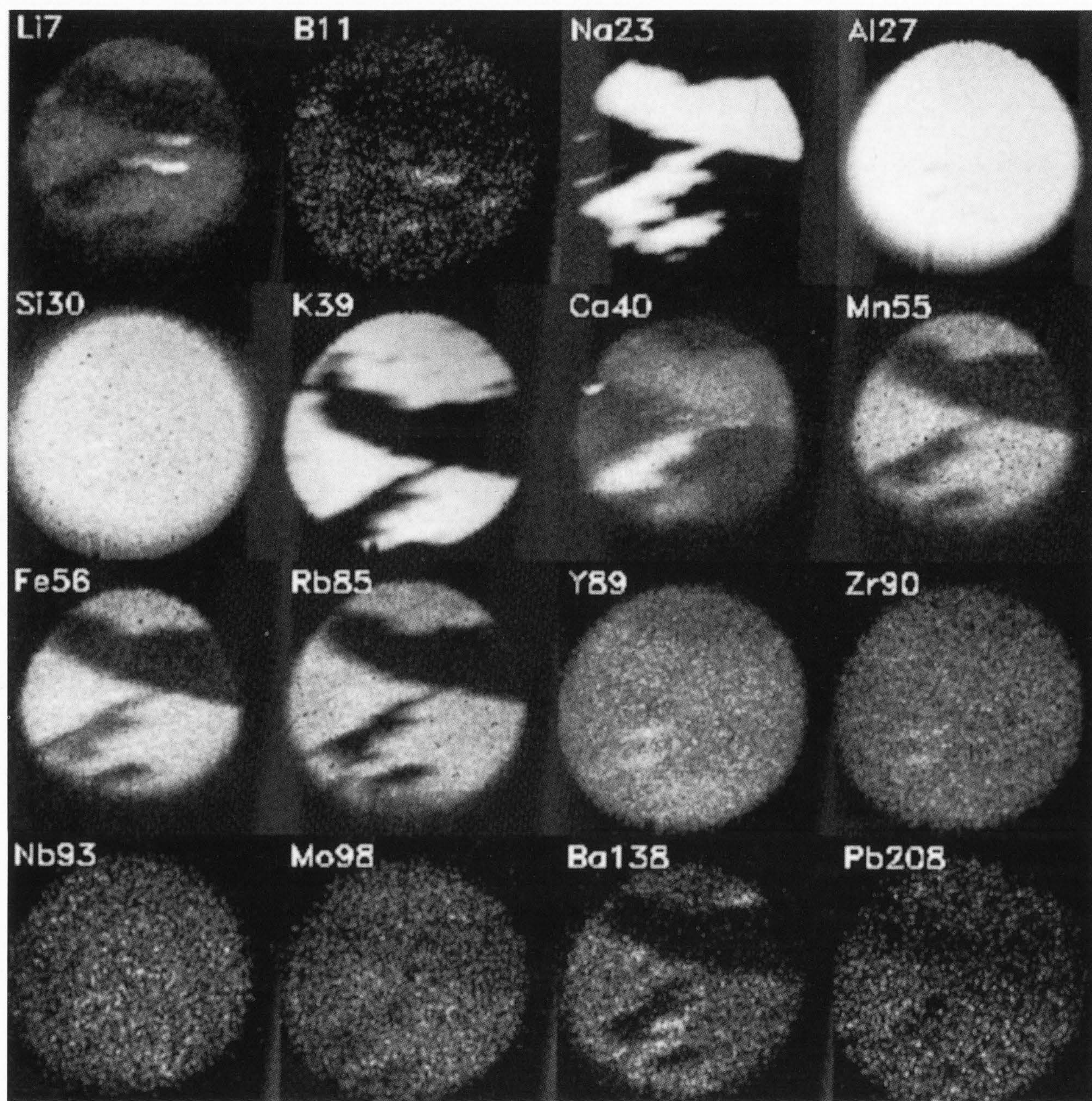

Figure 9. Secondary ion images of major and trace elements obtained from the same area as shown in Figure 8. Left to right, top to bottom: ^{7}Li, ^{11}B, ^{23}Na, ^{27}Al, ^{30}Si, ^{39}K, ^{40}Ca, ^{55}Mn, ^{56}Fe, ^{85}Rb, ^{89}Y, ^{90}Zr, ^{93}Nb, ^{98}Mo, ^{138}Ba and ^{208}Pb.

---

is true only for the K, and to a lesser extent for the Ca and Ti images. In contrast, the Mn, Fe, Sr, Rb, etc., maps show totally different distributions of these elements. The reason for this is the large difference in penetration depth for photons versus electrons and heavy ions. Whereas in SIMS only the top 10-100 nm of the material is being sampled (depending on the sputter time and beam intensity), an electron beam of 25 kV will penetrate approximately 3-5 μm into the material and characteristic X-rays will emerge from a pear-shaped interaction volume of comparable size. For high energy photons, however, the penetration depth is much larger. For example, the 1/e extinction length of photons of energy 5, 10 and 20 keV in the K-feldspar phases are

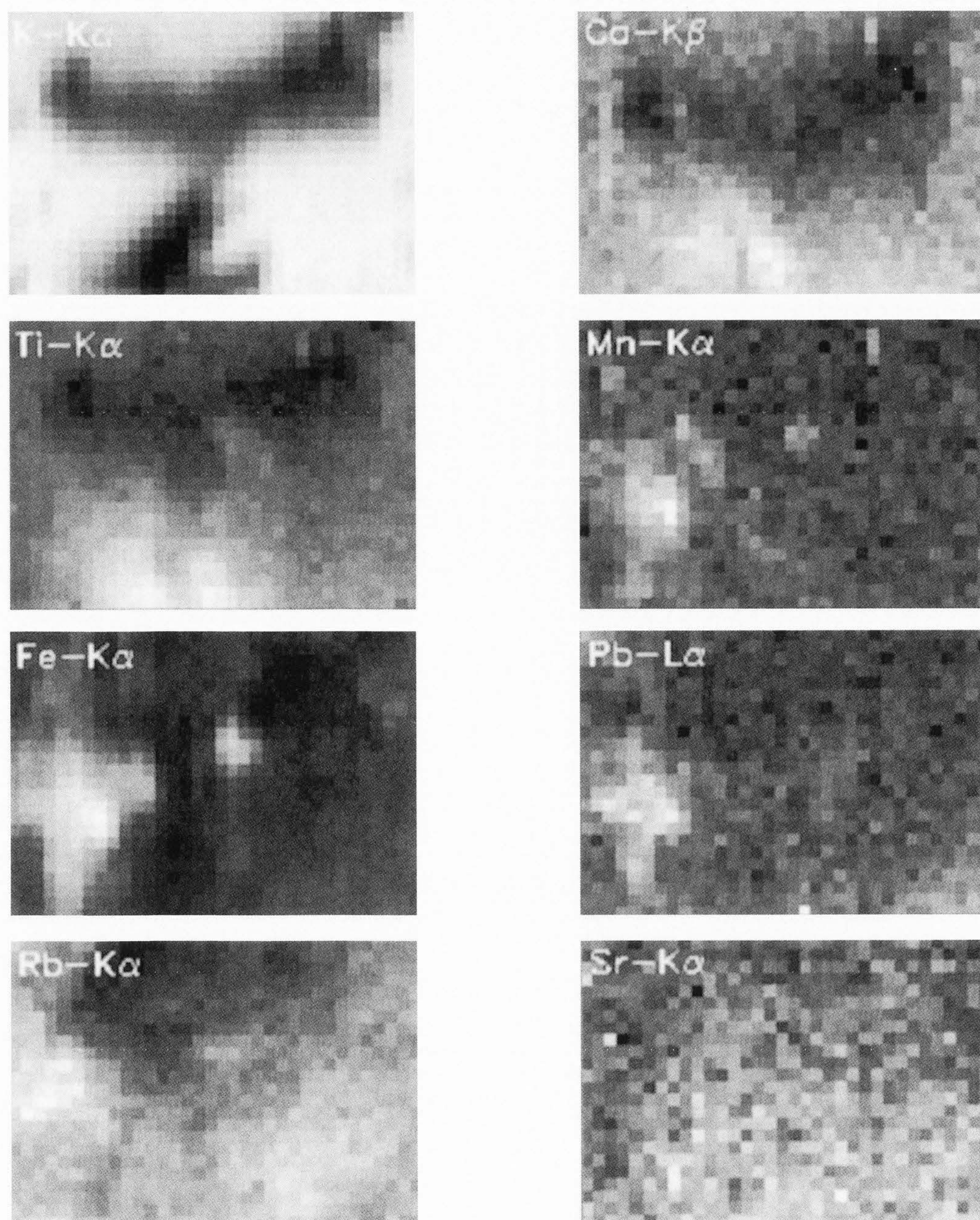

Figure 10. Synchrotron radiation induced X-ray maps of the area shown in Figure 8. Left to right, top to bottom: K-K_α, Ca-K_β, Ti-K_α, Mn-K_α, Fe-K_α, Pb-L_α, Rb-K_α, Sr-K_α.

18, 126 and 952 μm, respectively. Accordingly, by means of the white synchrotron spectrum (which extends beyond 40 keV), a layer of material of the order of 1 to 2 mm is excited. Whereas K-K_α radiation (3.312 keV) can only escape from the topmost 10 μm thick layer, the much more energetic Rb-K_α characteristic photons (13.375 keV) still have a probability of 37 % of reaching the detector when they originate from a depth of 300 μm. In this way, instead of only visualising the two-phase structure on the upper surface of the grain, the high energy μ-SRXRF elemental maps yield information on structures situated deeper into the material.

In a number of application areas of synchrotron radiation, the high penetration power of energetic photons is used advantageously. For example, by means of

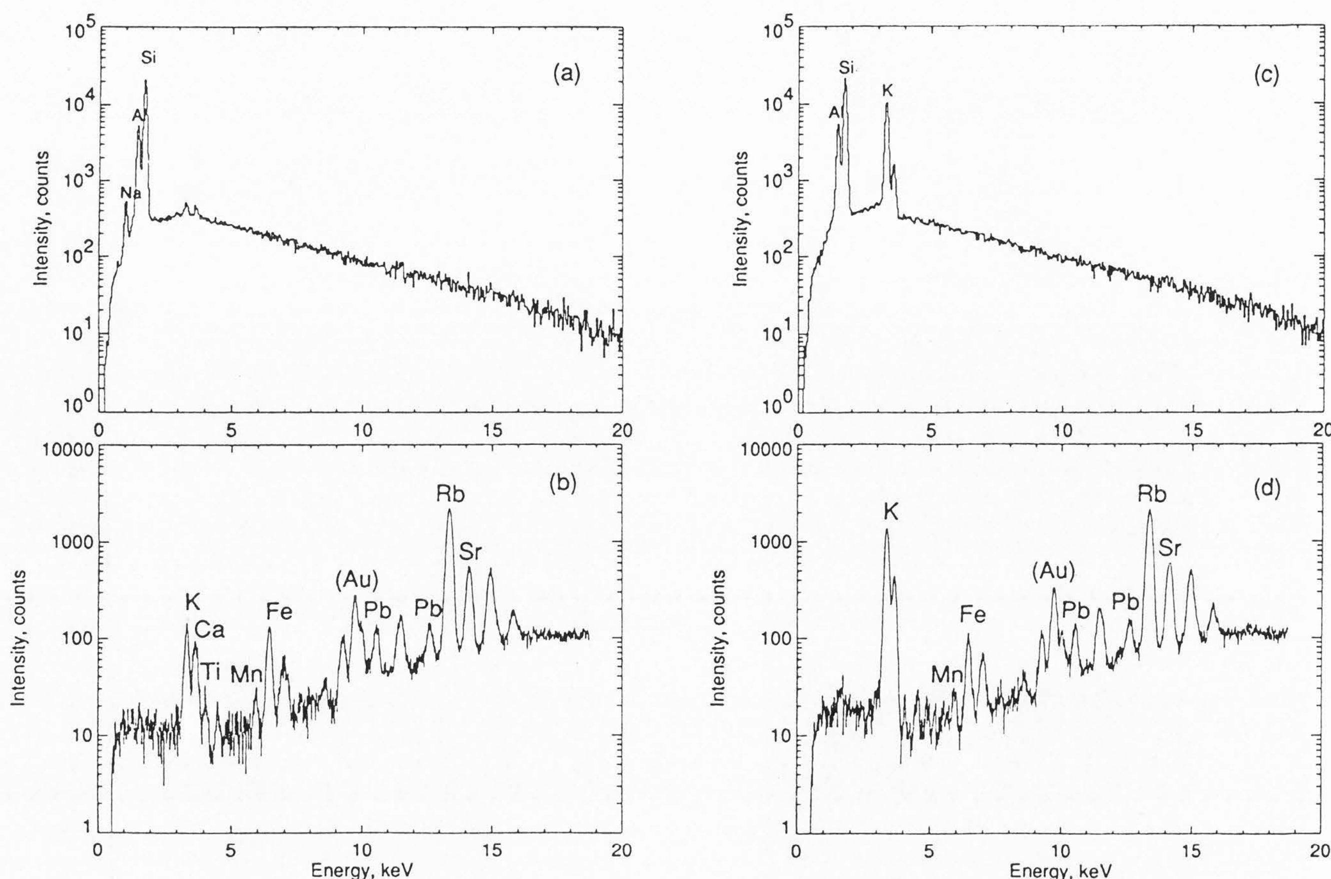

Figure 11. Electron and photon induced X-ray spectra of the albite and K-feldspar phase of the microcline perthite. Albite phase: (a) EPXMA spectrum, (b) μ-SRXRF spectrum; K-feldspar phase: (c) EPXMA spectrum, (d) μ-SRXRF spectrum.

CMT and radiation of 60 keV obtained from a 5T superconducting wiggler, Jones *et al.* (1992) were able to visualise the internal structure and density differences in a rat femur in which an orthopedic implant (a 1 mm stainless steel pin) was cemented, yielding information on the implant-bone interface in a non-destructive way. Frantz *et al.* (1988) used μ-SRXRF for probing fluid inclusions in quartz and could determine trace elements inside inclusions buried 20 to 100 μm below the surface.

On the other hand, the penetrative character of the radiation can also cause problems regarding the quantification of elemental μ-SRXRF maps. A simple example illustrates this. A 15-20 μm diameter Fe-rich inclusion is visible at the center of the Fe-K_α map of Figure 10. A similar structure, though less clear is discernable in the Ti, Mn and Rb images. The inclusion is located below the surface of the mineral, as it is not visible in the SIMS maps of the same region. If for simplicity, the characteristic Fe radiation is assumed to be mainly induced by radiation of average energy $E_o = 10$ keV and to originate from a particular (equivalent) depth d, the Fe concentration c_{Fe} in the inclusion is related to the detected Fe-K_α intensity I_{Fe} according to:

$$I_{Fe} = G\ Q_{Fe}\ c_{Fe}\ A_{Fe}\ I(E_o)\ t = S_{Fe}\ c_{Fe}\ A_{Fe}\ t \quad (1)$$

where G is an instrument specific constant (the geometry factor), Q_{Fe} is the production cross section for Fe-K_α radiation, A_{Fe} is an absorption factor and t is the measuring time. $I(E_o)$ is the intensity of the primary beam. S_{Fe} is called the sensitivity factor for Fe and was experimentally determined using a NIST SRM 1833 thin glass film standard. As, under the above assumptions, the absorption factor A_{Fe} is dependent on the depth of the inclusion beneath the surface d:

$$A_{Fe} = \exp\ \{-\rho\ d\ 1.42\ [\mu(E_o) + \mu(E)]\}, \quad (2)$$

Table 5. Calculated maximum Fe concentration in the Fe-rich inclusion shown in Figure 12 as a function of the assumed depth of the inclusion in the mineral (see text for details).

Equivalent Inclusion Depth d (μm)	Maximum Fe Concentration c_{Fe} ($\mu g/cm^2$)	Absorption Factor A_{Fe} (see eq. 2)
0	3.9 ± 0.1	1.0
10	5.5 ± 0.1	0.7
20	7.7 ± 0.2	0.5
30	11.1 ± 0.3	0.35
40	15.4 ± 0.4	0.24

it is clear that d must be known in order to convert the Fe-K_α intensity map of Figure 12 into a concentration image. As the information cannot be derived from the X-ray data themselves, this presents a fundamental limitation to quantitative μ-SRXRF analysis of heterogeneous samples. The extent of the error that is made if an incorrect value of d is employed can be estimated from Table 5, where the influence of employing various values of d chosen between 0 μm and 40 μm (the 1/e extinction depth for Fe-K_α radiation) on the maximum Fe concentration in the inclusion are listed. The calculations were done assuming the inclusion to be buried in the albite phase.

The penetration of photons into the solid also has an influence on the lateral resolution in the acquired images. In Figure 13, cross sections of the ^{39}K ion and K-K_α X-ray maps are plotted along a line perpendicular to the long axis of the exsolution lamella (see black line in Figure 3). Employing a 10-90% criterion, from this plot, the width of the interface between the two phases derived from the SIMS, EPXMA and μ-SRXRF data is estimated to be 3, 5 and 12 μm, respectively. Taking diffusion of K into the albite phase into account and the lateral resolution of the SIMS instrument (< 1 μm), the first number can be considered as a reliable estimate of the true interface width. The interface width derived from the EPXMA and μ-SRXRF data are larger as a result of the extended interaction volumina of the electron and photon beam, respectively. The 5 μm interface width found in the EPXMA case is in accordance with the expected size of the interaction volume for a 25 kV electron beam (about 3.5 μm) in this case. In constrast, in the μ-SRXRF case, although a beam of 5 x 5 μm^2 dimensions was used (measured by scanning over the edge of a thin gold edge deposited onto kapton foil), an interface width larger by a factor of 2 to 3 is obtained.

This broadening cannot be explained by the scatter "halo" of the beam. An explanation which is in accordance with the image data of Figures 9 and 10 is schematically shown in Figure 13b. If the albite exsolution lamella in the center of the image is assumed to have a thickness of the order of 10 to 15 μm, before the

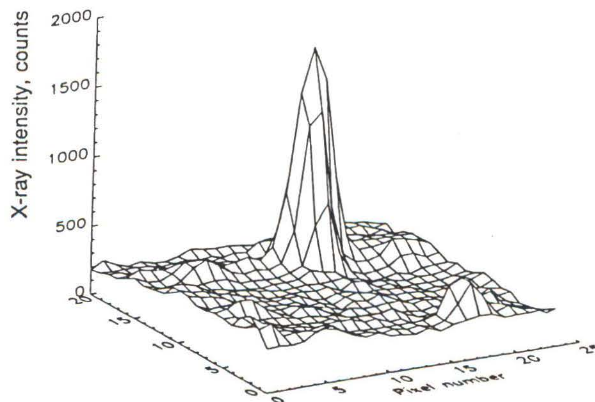

Figure 12. Surface plot of the Fe-K_α intensity near the location of the Fe-rich inclusion.

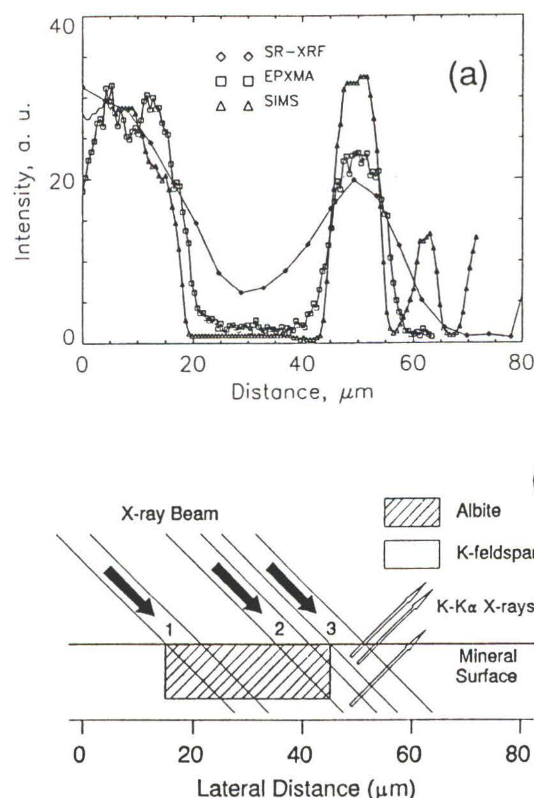

Figure 13. (a) Cross sections of the K-K_α X-ray and ^{39}K ion images along the black line shown in Figure 3. (b) In-depth model of the structure of the albite lamella; the position of the photon beam at various locations, before, at and after the edge is also shown.

primary beam reaches the edge of the lamella (position 2) on the mineral surface, energetic photons will pass through the side of the albite layer and excite the K-rich phase. As a result, a gradual increase of the K-K_α intensity can be observed until the beam reaches position 3. In reality, the model of Figure 13b is probably too simplistic in the sense that the edge between the Na and K-rich phases may not be a straight line or perpendicular to the surface of the mineral. It should be noted that in common mineralogical applications polished thin sections of 30 μm are usually employed and that, in such samples, the extent of the above mentioned broadening phenomenon may be somewhat reduced. Nevertheless, in these types of thin sections, a significant degradation of the lateral resolution can be observed experimentally.

μ-SRXRF at Third Generation Synchrotron Sources

A number of the above discussed limitations of μ-SRXRF can be eliminated by using more intense photon sources. At currently operating storage rings, this can be done by using wiggler radiation instead of X-rays originating from a bending magnet. Rivers *et al.* (1992) have discussed μ-SRXRF experiments at the 5T superconducting wiggler of NSLS beamline X17B1. Next to the advantage brought by the higher intensity of the source, they point out that, as a result of the higher divergence of the wiggler beam in the vertical plane, a poorer degree of polarisation of the microbeam is obtained than at the X26A bending magnet beamline.

An alternative is to employ radiation from one of the third generation synchrotron rings now currently under construction in Japan (SPring-8 in Harima), the US (APS at Argonne National Laboratories, Illinois) and in Europe (ESRF in Grenoble, France). For the latter facility, whose test phase has already started, we have estimated the expected improvement in flux density and achievable MDL's when a collimated X-ray microprobe would be installed at a 0.8 T bending magnet beam line. The predictions are based on a detailed Monte Carlo simulation of the interaction of a polarised, polychromatic photon beam with sample atoms (Vincze *et al.*, 1993a; Janssens *et al.*, 1993b). The details of these calculations, which also include a comparison of the performance of optical devices for generating high energy X-ray microbeams other then pin holes, are presented elsewhere (Vincze *et al.*, 1993b).

In general, however, compared to the μ-SRXRF spectrometer at the NSLS X26A beamline, an increase in flux density by a factor of 50 is obtained. As the critical energy of the ESRF (19.6 keV) is much higher than that of the NSLS (5.9 keV), the ESRF spectrometer is also expected to be more sensitive for determination of heavier elements than the NSLS instrument (van Langevelde *et al.*, 1992). The 50-fold increase in flux-density also implies that, at the ESRF, approximately the same flux will be concentrated into a 2 x 2 μm^2 area as is currently available in an 8 x 8 μm^2 spot at the NSLS.

In terms of the above discussed applications, this means that it will be possible to analyse particles with sizes down to 1-2 μm diameter or alternatively to characterise 50 times more particulates in the size range 5-20 μm in the same time as currently required at the NSLS. With respect to trace element imaging applications, e.g., for the investigation of biological materials, a 2 x 2 μm^2 beam will allow the visualisation of the distribution of chemical elements in single (living) cells. If large beam sizes are employed, a substantial reduction in acquisition time can be expected. For example, the time necessary to acquire the X-ray maps of Figure 10 would reduce from 12 h to $\sim$15 min, making the X-ray microprobe a much more interactive type of analytical technique than currently is the case.

Conclusions

In this work, a comparison was made between μ-SRXRF and more conventional microanalytical techniques such as EPXMA and SIMS. The applicability of μ-SRXRF to two typical microanalytical problems, namely the characterisation of individual particles and the mapping of trace elements in solids was evaluated. It was concluded that μ-SRXRF is a valuable method for analysis of trace, minor and major elements and that it can be used profitably in parallel with electron- and ion-beam methods.

With respect to the analysis of microscopical particles, one can conclude that using EPXMA and white light μ-SRXRF, the same major particle classes can be identified, even when only a limited number of particles are analysed. Whereas by means of μ-SRXRF information on the trace constituents can readily be obtained, the applicability of the method is limited by the long counting times which are needed to extract this information from each particle and by the fact that only coarse mode aerosols can be analysed. These limitations, however can be overcome by using more brilliant X-ray sources. Another limitation is the very low sensitivity of current μ-SRXRF instruments for low Z elements.

A complementary scheme of particle characterisation in which both μ-SRXRF and EPXMA are used appears most promising. In such a scheme, first automated EPXMA could be used to identify and determine the abundance and major composition of the various groups in the aerosol population; in a second phase, μ-SRXRF could be employed to obtain (more accurate) information on the major and trace level composition of some or all the particle classes by analysing a limited number of

aerosols.

The applicability of μ-SRXRF for accurate mapping of trace elements with atomic number > 20 in a non-destructive way is evident. However, current analytical procedures which can reliably convert X-ray images collected from heterogeneous, non-thin samples into concentration maps still lack sophistication. Quantitative analysis of the image data in this type of sample is primarily hampered by the high penetration of the primary photon beam, which in this type of sample also limits the lateral resolution of μ-SRXRF to 10-20 μm in the 45°/45° measuring geometry. In this respect, the evaluation of the (dis)advantages of using other geometries (such as 5°/85° or even 0°/70°), which do not yield optimal sensitivity/MDL's but a higher lateral resolution, may be of interest. Similarly, the combination of two-dimensional mapping with differential absorption and/or fluorescent microtomography may provide a solution to these quantification problems. The problem obviously vanishes if sufficiently thin specimen are employed.

Predictions of the performance of a white light μ-SRXRF spectrometer installed at a bending magnet of a third generation storage ring indicated improvements in flux density by a factor of 50, elimitating some of the above-mentioned limitations of present day μ-SRXRF instruments.

Acknowledgements

K.J. is a Fellow of the Belgian National Science Fund, Brussels, Belgium; this work was sponsored by FKFO (Brussels) Grant Nr. 2009291N. The authors are indebted to W. Dorrine and W. Saenen for assisting with the EPXMA work and to J. Van Vooren and W. Van Hoolst for the SIMS measurements. We would like to thank P. Artaxo for providing us with the Antarctic aerosol particle samples. This research was also supported by the U.S. Department of Energy, Office of Basic Energy Sciences, Chemical Sciences Division under Contract No. DE-AC02-76CH00016. M.R. wishes to thank the National Science Foundation (N.S.F.) for support through grant No. EAR89-14669.

References

Artaxo P, Andrade F, Maenhaut W (1990) Trace elements and receptor modelling of aerosols in the Antarctic Peninsula. Nucl. Instr. Meth. **B43**, 383-387.

Artaxo P, Rabello MLC, Watt F, Grime G, Swietlicki E (1993) Nuclear microprobe analysis and source apportoinment of individual atmospheric aerosol particles. Nucl. Instr. Meth. **B75**, 749-752.

Bavdas M, Knöchel A, Ketelsen P, Pertersen W, Gurker N, Salehi MH, Dietrich T (1988) Imaging multi-element analysis with synchrotron radiation excited X-ray fluorescence radiation. Nucl. Instr. Meth. **A266**, 308-315.

Baryshev VB, Kulipanov GN, Zavtsev EI, Terekhov YV, Kalyuzny VI (1987) Sensitive X-ray fluorescence analysis of geological samples using synchrotron radiation. Nucl. Instr. Meth. **A261**, 279-283.

Bernard P, Van Grieken R, Eisma D (1986) Classification of estuarine particles by automated electron microprobe analysis and multivariate cluster techniques. Envir. Sci. Technol. **20**, 467-473.

Birks J, Seebold RE, Batt AP, Grosso JS (1964) Excitation of characteristic X-rays by protons, electrons and primary X-rays. J. Appl. Phys **35**, 2578-2581.

Bodhaine BA, Deluisi JJ, Harris JM, Houmere P, Bauman S (1987) Pixe analysis of south pole aerosol. Nucl. Instr. Meth. **B22**, 241-247.

Bos AJJ, Vis RD, Verheul H, Prins R, Davies ST, Bowen DK, Makjanic J, Valkovic V (1984) Experimental comparison of synchrotron radiation with other modes of excitation of X-rays for trace element analysis. Nucl. Instr. Meth. **B3**, 232-239.

De Boer DKG, Van den Hoogenhof WW (1992) Total reflection X-ray fluorescence of single and multiple thin-layer samples. Spectrochimica Acta **B46**, 1323-1331.

Frantz JD, Mao HK, Zhang Y, Wu, Y, Thompson A, Underwood J, Giauque R, Jones K, Rivers M (1988) Analysis of fluid inclusions by X-ray fluorescence using synchrotron radiation. Chemical Geology **69**, 235-244.

Goossens D, Van't Dack L, Gijbels R, (1989) Ion-microprobe analysis of rock-forming minerals from the Carnmenellis Granite. In: Water-Rock Interaction. Miles DL (ed.). Balkema, Rotterdam/Brookfield, 267-270.

Goshi Y, Aoki S, Iida A, Haykawa S, Yamaji H, Sakurai K (1987) Micro X-ray fluorescence using synchrotron radiation. Jpn. J. Appl. Phys. **26**, L1260-L1266.

Kwiatek WM, Long GJ Reuhl KR, Hanson AL, Jones KW, Pounds JG (1987) Distribution of Fe, Cu, Zn and Hg in the mouse cerebellum. Toxicologist **7**(1), 302a-307a.

Janssens K, Van Borrn W, Van Espen P (1988) Increased accuracy in the automated interpretation of large EPMA data sets by the use of an expert system. NBS J. of Research **93**(1), 260-264.

Janssens K, van Langevelde F, Adams FC, Vis RD, Sutton SR, Rivers ML, Jones KW, Bowen DK (1992a) Comparison of synchrotron X-ray microanalysis with electron and proton microscopy for individual particle analysis. Adv. X-ray Anal. **38**, 1615-1619.

Janssens K, Adams F, Rivers ML, Jones KW (1992b) Analysis of individual microscopic particles by means of synchrotron radiation induced X-ray micro-

fluorescence. Proc. 27th MAS **27**, 1766-1767.

Janssens K, Vincze L, Adams F, Jones KW (1993a) X-ray microanalysis. Anal. Chim. Acta. **283**, 98-119.

Janssens K, Vincze L, Van Espen P, Adams F (1993b) Monte Carlo simulation of conventional and synchrotron energy-dispersive X-ray spectrometers, X-ray Spectrom. **22**, 234-243.

Jones KW, Gordon BM (1989) Trace element determinations with synchrotron-induced X-ray emission. Anal. Chem. **61**, 341A-358A.

Jones KW, Gordon BM, Hanson AL, Hastings JB, Howells MR, Kraner HW, Chen JR (1984) Applications of synchrotron radiation to elemental analysis. Nucl. Instr. Meth. **B3**, 225-228.

Jones KW, Spanne P, Schidlovsky G, Xue D, Bochnan R, Rabinowits M, Hammond P, Bornschein R, Hoeltzel D (1992) Calcified-tissue investigations using synchrotron X-ray microscopy. In: X-ray Microscopy III. Michette A, Morrison G, Buckley C (eds.). Springer Verlag, Berlin, 306-310.

Mazzolini AP, Legge GJF, Palaghy CK (1981) The distribution of trace elements in mature wheat seed using the melbourne proton microprobe. Nucl. Instr. Meth. **191**, 217-220.

Raeymaekers B (1986) Characterisation of particles by automated electron probe microanalysis. Ph. D. Thesis. University of Antwerp.

Rivers ML, Sutton SR, Jones KW (1992) X-ray fluorescence microscopy of geological samples. In: X-ray Microscopy III. Michette A, Morrison G, Buckley C (eds.). Springer Verlag, Berlin, 212-216.

Spanne P, Rivers ML (1987) Computerized microtomography using synchrotron radiation from the NSLS. Nucl. Instr. Meth. **B24/25**, 1063-1067.

Sparks CS (1980) Photon-based vs. charged particle based microanalysis. In: Synchrotron Radiation Research, Winick H, Doniach S (eds.). Plenum Press, New York, 173-182.

Thompson AC, Underwood JH, Wu Y, Giauque RD, Jones KW, Rivers ML (1988) Elemental measurements with an X-ray microprobe of biological and geological samples with femtogram sensitivity. Nucl. Instr. Meth. **A266**, 318-322.

Török Sz, Szökefaldvi-Nagy Z, Sándor S, Baryshev VB, Zolotarev KV, Kulipanov GN (1989) Comparison of X-ray emission analysis sensitivity under various techniques of excitation in biological and environmental studies. Nucl. Instr. Meth. **A282**, 499-501.

Traxel K (1988) Microscopic particle induced X-ray emission. Nucl. Intr. Meth. **A268**, 567-578.

Van Espen P (1984) A program for processing analytical data (DPP). Anal. Chim. Acta **165**, 31-49.

Van Espen P, Janssens K, Nobels J (1986) AXIL, Software for processing of complex X-ray spectra. Chemolab. **1**, 109-114.

van Langevelde F, Bowen DK, Tros GHJ, Vis RD, Huizing A, de Boer DKG (1990) Ellipsoid X-ray focussing for synchrotron radiation microprobe analysis at the SRS, Daresbury, U.K. Nucl. Instr. Meth. **A292**, 719-725.

van Langevelde F, Janssens K, Adams F, Vis RD (1992) Prediction of the optical characteristics and analytical qualities of an X-ray fluorescence microprobe at the European Synchrotron Radiation Facility (Grenoble). Nucl. Instr. Meth. **A317**, 383-393.

Vincze L, Janssens K, Adams F (1993) A general Monte-Carlo simulation of ED-XRF spectrometers, Part I: Unpolarised radiation homogeneous samples. Spectrochimica Acta **B48**, 553-573.

Vincze L, Janssens K, Adams F (1993) Micro-focus X-ray optics for synchrotron radiation induced X-ray fluorescence at the ESRF Inst. Phys. Conf. Ser. No. **130**, 613-616.

Vis RD (1988) Proton induced X-ray emission. Scanning Microscopy **2**, 977-985

Discussion with Reviewers

E. Swietlicki: One major limitation precluding the general use of SRXRF micro-analysis is the cost of the "X-ray tube", i.e., the synchrotron. There is roughly a one order of magnitude increase in cost for the equipment needed for implementing in turn EPXMA, μ-PIXE and μ-SRXRF. For this reason, it is not enough for μ-SRXRF to achieve results comparable to EPXMA, SIMS and μ-PIXE. At least in some areas of application, it will have to excel over these techniques, if not to remain an exclusive and quaint analytical technique. Can you pinpoint such typical μ-SRXRF applications?

Authors: Considering the fact that large physical installations such as synchrotron rings are not built for the sole purpose of being able to perform μ-SRXRF, the extra costs for realising a μ-SRXRF beamline, even at third generation synchrotron sources such as the ESRF or the APS are of the same order of magnitude as the cost of an accelerator employed for PIXE.

The areas of science where the unique qualities of μ-SRXRF are being exploited are those where (**a**) very precious and/or sensitive materials are being studied (cosmochemistry, archeometry, structural biology, *in vivo* analysis) and where damage to the samples must be minimised; and (**b**) low concentrations of heavy elements (e.g., rare earths) need to be determined in a reliable way and (**c**) when combined with XANES measurements, information on the distribution of chemical elements in a sample needs to be complemented with data on the chemical state of some of these elements. Next to that, at undulator lines of third generation sources, the

sensitivity of μ-SRXRF employing monochromatic forms of excitation will also be significantly better than that of μ-PIXE. The combination of this 10-100 ppb level sensitivity with the quantitative reliability of XRF will make μ-SRXRF an non-destructive microanalytical technique without real competitors.

E. Swietlicki: You state that you are limited in lateral resolution to about 5 x 5 μm^2. You discuss the improvements attainable on the next synchrotron generation. What then are the limitations imposed by the design of the beam-line, and what improvements can be made here to improve on the performance of μ-SRXRF?
Authors: At the NSLS X26A beam line, the lateral resolution of 5 x 5 μm^2 is determined by the available flux density; using smaller beams is possible but at the expense of collimating away a considerable part of the primary photon flux. When moving to third generation synchrotron rings and by using smaller, more brilliant X-ray sources (undulator lines) together with focussing optics, a increase in flux and flux density by several orders of magnitude can be expected. This will result in a reduction of the beam sizes to the 1 x 1 μm^2 level, next to a substantial improvement in sensitivity, with MDL values situated in the 1-100 ppb range for elements heavier than Ca. The performance of μ-SRXRF spectrometers at these sources very strongly depends on which microfocussing optical configuration actually will be used. An important improvement in the accuracy of the technique will also result from the use of monochromatic primary radiation rather than the white synchrotron light.

E. Swietlicki: Figure 1 shows the cross sections for production of characteristic X-rays when using SR X-rays, electrons and protons as exciting particles. More important are the attainable detection limits for typical samples. Would a figure depicting detection limits show a similar picture?
Authors: This question already has been addressed in Janssens *et al.* (1992a) for the case of small particles. The detection limits of μ-SRXRF are not only determined by the production efficiency of the fluorescent radiation but also by the processes giving rise to the background. In the case of polychromatic radiation, an efficient excitation of most elements in the periodic table is achieved, but also a continuous scatter background can be observed in the XRF spectra; because the exciting radiation is nearly completely linearly polarised in the synchrotron ring plane, the intensity of this continuum is significantly reduced relative to situations where unpolarised radiation is employed (as in conventional XRF apparatus). Thus, for polychromatic forms of excitation, fairly uniform MDL levels at or just below the 1 ppm level are achieved.

When monochromatic radiation is employed, only for the elements whose absorption edge is situated just below the energy of the primary radiation, very efficient excitation is achieved; since on the other hand virtually background-free XRF spectra are obtained (except for the scatter peaks); this type of excitation results in sub-ppm MDL's.

E. Swietlicki: For the individual aerosol particles, the concentrations are given in ppm, which implies that the matrix is known. Since μ-SRXRF does not measure the low-Z elements, I presume the composition of each particle has to be assumed beforehand as for the sea-spray particles, where you assume a NaCl matrix. What would be the procedure for other types of particles, say from soil dust? Could you outline the procedure used? Were corrections made for the attenuation of incoming and emitted X-rays and for particle size and shape?
Authors: For the Antarctic samples, most particles were larger than the beam's footprint; accordingly, the excitation geometry could be approximated by that of an NaCl film of the same thickness. Using this model, the attenuation of the incoming and emitted X-rays was corrected for. No corrections for other secondary phenomena (e.g., enhancement) were applied.

For the case of particles of which the matrix is unknown, two options exist for quantification: (a) employ the average matrix composition of the particle class the particles in question belong to. This approach implies pre-investigations of the aerosols samples using another microanalytical technique such as EPXMA. See also Janssens *et al.* (1992b) for more details; and (b) when monochromatic radiation is employed, the intensity of the scatter peaks can be used to estimate the total mass of the particle; the ratio of the Compton to Rayleigh peak intensities provides information on the average atomic number of the particle matrix and can be used in attenuation corrections. This is a standard procedure in bulk XRF. The use of monochromatic radiation of small object analysis, however, will only become possible in routine practice at third generation sources.

In view of the highly penetrative character of the incoming radiation, the influence of particle shape is minimal, unless very extreme shapes (flat disks, needles, ...) are concerned.

Reviewer 2: The comparison between EPXMA and SRXRF shown in the figures may give the impression that EPXMA is of poorer sensitivity for high-Z elements or characteristic X-rays of high energy. Is this correct if one uses wavelength dispersive spectroscopy?
Authors: In the case of energy dispersive (ED) detection, the sensitivity of EPXMA and current-day μ-

SRXRF spectrometers is situated at the 100 and 1 ppm level, respectively. When switching to wavelength dispersive (WD) detectors, a 5-10 fold improvement in the resolution may result in a 2-3 fold improvement increase in MDL's. However, this increase in sensitivity may not be fully realised in view of the lower efficiency of wavelength dispersive detectors. Whatever the improvement in sensitivity may be, both μ-SRXRF and EPXMA spectrometers can be equipped with both ED and WD detectors. In the μ-SRXRF case, WD detection has the advantage that certain overlapping peaks can be resolved while the detector is not saturated by very intense matrix lines or scatter peaks.

Reviewer II: Are there any investigations of SRXRF as applied to total reflection fluorescent X-ray analysis which has been attracting much attention in the semiconductor industry?
Authors: Glancing angle excitation is difficult to combine with laterally resolved measurements with micrometer level resolution. By means of careful detection collimation, however, a lateral resolution in the mm range is achievable (e.g., for inspection of large Si wafers). Depth profiling using variable angle glacing incidence excitation has been reported, both with conventional and with synchrotron sources (see, e.g., De Boer *et al.*, 1992).

R. Vis: It is possible to avoid X-rays from deeper layers in the 45°/45° geometry (Figure 13) by placing an absorber on top of the specimen very close to the incoming beam? In this way, one blocks the outgoing X-rays from deeper layers on their way to the detector. A very precise collimator to collimate the beam placed immediately on top of the sample will do the same job.
Authors: An absorber could be used but might be rather cumbersome to keep in exactly the same position relative to the X-ray beam and yet very close to the (moving) sample. On the other hand, the sample itself can act as absorber if not the usual 45°/45° geometry is employed but, say, a 85°/5° arrangement. Of course, since the path of the emitted X-rays on their way to the detector becomes much longer, the probability for all secondary phenomena (i.e., absorption, enhancement, second order scattering) increases, complicating the quantification procedure.

R. Vis: It is remarkable that particle clustering during hierarchical cluster analysis is better in intensity space than in concentration space. Even if a sysumatic error occurs and concentrations are assigned wrongly but in a consistent way, one expects still the same clustering of the data. Only if the sensitivity or calibration factors to convert intensity to concentration are varying from particle to particle one might obtain the results you described. Please comment on this varying sensitivity.
Authors: The clustering technique which was employed here employs the euclidian distance in the multivariate space between the various objects to be classified (in this case particles). The distances between all couples of objects are used to decide which two objects can be "fused" together into a cluster; the cluster subsequently starts to act as a single object, etc. As such, the classification in intensity space occurs mainly on the basis of the most intense X-ray peaks in a spectrum, which are also the most precisely known "properties" of an object.

When one switches from intensity to concentration space, apart from possible errors in the quantification, the dynamic range of the "properties" is more compressed because of the **inter-element variation** of the μ-SRXRF sensitivity factors. Due to the transformation, classification must then occur on the basis of the major element data available for each particle which (in this case) cannot very precisely be estimated from the XRF data, while the weight of the trace element content in the classification scheme is reduced. The classification works less well in concentration space than in intensity space not as a result of variation of elemental sensitivity **between particles** but rather as the result of the sensitivity variation **among elements** and the resulting uncertainty on the major composition of the particles.